



MedSora: Optical Flow Representation Alignment Mamba Diffusion Model for Medical Video Generation

Zhenbin Wang, Lei Zhang^(✉), Lituan Wang, Minjuan Zhu, Zhenwei Zhang

Machine Intelligence Laboratory
College of Computer science, Sichuan University
Chengdu, Sichuan Province, China

wangzhenbin@stu.scu.edu.cn, leizhang@scu.edu.cn

Abstract

Medical video generation models are expected to have a profound impact on the healthcare industry, including but not limited to medical education and training, surgical planning, and simulation. Current video diffusion models typically build on image diffusion architecture by incorporating temporal operations (such as 3D convolution and temporal attention). Although this approach is effective, its oversimplification limits spatio-temporal performance and consumes substantial computational resources. To counter this, we propose *Medical Simulation Video Generator (MedSora)*, which incorporates three key elements: *i*) a video diffusion framework integrates the advantages of attention and Mamba, balancing low computational load with high-quality video generation, *ii*) an optical flow representation alignment method that implicitly enhances attention to inter-frame pixels, and *iii*) a video variational autoencoder (VAE) with frequency compensation addresses the information loss of medical features that occurs when transforming pixel space into latent features and then back to pixel frames. Extensive experiments and applications demonstrate that *MedSora* exhibits superior visual quality in generating medical videos, outperforming the most advanced baseline methods. Further results and code are available at <https://wongzbb.github.io/MedSora/>.

1 Introduction

With the development and integration of technologies such as diffusion (Ho et al., 2020; Sohl-Dickstein et al., 2015), multimodal (Radford et al., 2021; Ramesh et al., 2021), pre-trained models (Brown et al., 2020), and model fine-tuning (Hu et al., 2021; Li & Liang, 2021), artificial intelligence generated content (AIGC) has achieved remarkable progress, sparking widespread interest in interdisciplinary medical fields. Ranging from image reconstruction (Liu et al., 2023) and translation (Wang et al., 2024) to the generation of virtual cases and the creation of simulation data (Özbey et al., 2023), AIGC underpin numerous innovations. This has significantly advanced the frontiers of computer-assisted diagnosis and precision medicine. Recently, advances in video generation models (Blattmann et al., 2023; An et al., 2023; Huang et al., 2024) have propelled AIGC to new heights. However, due to the considerable complexity and significant resource demands of clinical video generation, research in this area remains in its nascent stages. In this context, our work aims to explore whether it is possible to create temporally coherent and realistic clinical medical videos.

Significant progress has been made in generating realistic medical images using generative adversarial networks (GANs) (Goodfellow et al., 2014) and diffusion models (Rombach et al., 2022). However, video is composed of pixel arrays spanning both temporal and spatial dimensions, necessitating meticulous attention to fine temporal dynamics and the maintenance of temporal consistency across frames. Consequently, generating stable, high-quality videos is a non-trivial task. To achieve this, most recent works in computer vision attempt to extend the spatial self-attention mechanism of images to spatio-temporal self-attention (Khachatryan et al., 2023; Qi et al., 2023), using pseudo-3D (Singer et al., 2022) or serial 2D+1D convolutions (Xing

^(✉)The corresponding author.

et al., 2024a) to apply image diffusion models to video generation. To the best of our knowledge, the sole existing study in the medical field on video generation employs the spatio-temporal self-attention (Li et al., 2024). Those strategies integrate features from patches across different video frames via an expanded attention or convolution module, as illustrated in Figure 1.

Despite their effectiveness in capturing contextual information across space and time, these methods have significant drawbacks: *i)* spatio-temporal self-attention requires each patch attends to all other patches in the video, which not only poses the risk of misdirecting the attention mechanism with patches that are irrelevant to video generation (Liu et al., 2022), but also significantly increases the computational complexity, presenting significant challenges in terms of resource allocation and maintaining cross-frame coherence, and *ii)* convolutional methods focus only on local areas and cannot capture the global receptive field, thereby reducing model performance. To mitigate these challenges, some recent works have incorporated Mamba (Gu & Dao, 2023; Dao & Gu, 2024) into video generation, they typically replace the original convolution or attention modules of GANs or diffusion models with Mamba (Gao et al., 2024; Mo & Tian, 2024), or merely alter the scanning order of patches (Park et al., 2024) without thorough exploration. These Mamba-based video generation models exhibit two primary limitations: *i)* existence of pixel-level bias. Recent advances in diffusion models for image generation illustrate that Mamba underperforms relative to certain Transformer in generating pixel-level data (Wang et al., 2024). And *ii)* absence of explicit spatio-temporal modeling. These models either maintain the same structural design of image generation models (Mo & Tian, 2024; Gao et al., 2024) or simplistically modify the sequence of video frames (Park et al., 2024), assuming it to suffice for spatio-temporal modeling. We aim to address these challenges by advancing our approach with an optimized design of spatio-temporal Mamba and attention blocks.

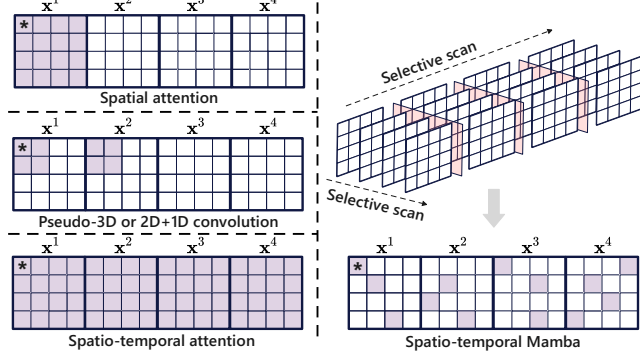


Figure 1: Illustration of spatial attention, pseudo-3D or 2D+1D convolution, spatio-temporal attention, and our spatio-temporal Mamba. x^k represents the feature map of the k -th video frame. Patches marked with '*' are computed together with the colored patches to aggregate their features.

Spatio-temporal self-attention frameworks typically model the content within each video frame before conducting temporal modeling of patches at corresponding positions across frames (Diba et al., 2023). However, this approach has a significant limitation as it presupposes linear motion of patches along the temporal axis. This assumption leads to inadequate mutual attention among patches following non-linear trajectories across frames. To overcome existing drawbacks, we propose a supervised, optical flow representation alignment method seamlessly integrated into the video diffusion model. By using optical flow (Fleet & Weiss, 2006; Shi et al., 2023) to implicitly control key features, our method addresses the visual consistency problems identified in previous work. A primary benefit is the facilitation of precise information transfer between frames through optical flow guidance, stabilizing the generated visual content throughout the video. Specifically, we initially employ a pre-trained optical flow estimation model (Teed & Deng, 2020) to determine the optical flow of the source video. Following this, a self-supervised foundation model (Caron et al., 2021) is utilized to extract key features of the optical flow from various perspectives. These key features are then sampled and leveraged to supervise the training of video diffusion model, without the addition of any extra training parameters.

Video generation models process high-dimensional videos as cubic arrays, necessitating substantial memory and computational resources, particularly for high-resolution and extended-duration videos. To reduce the computational load, numerous video diffusion models (Blattmann et al., 2023; An et al., 2023) are not trained on raw pixels, but first employ an autoencoder (Kingma & Welling, 2013) to project video frames into low-dimensional latent space and then model this latent distribution. However, the pre-train time-agnostic image autoencoder can distort the temporal information in the latent space (Zhou et al., 2022), i.e., the change $\Delta_z = z_i \rightarrow z_j$ from the i -th frame to the j -th

frame in the latent space suffers from frame consistency degradation or misalignment compared to the change $\Delta_x = x_i \rightarrow x_j$ in the original pixel space. To address this challenge, Lin et al. (2023) using additional modules, and Xiang et al. (2023a) retrained the decoder for image autoencoder. Researchers have recently begun training video autoencoders on large-scale video datasets (Yang et al., 2024). However, the limited availability of medical videos means that these video autoencoders have not been adequately trained on medical datasets. *We incorporate frequency compensation modules into the video VAE to preserve spatio-temporal consistency, particularly during the projection and reconstruction processes of medical videos under spectral constraints.*

The primary contributions of this paper are: *i)* proposing a novel video diffusion model framework that introduces spatio-temporal capabilities while minimizing resource requirements, featuring powerful spatio-temporal Mamba module and local attention mechanism. *ii)* optical flow representation alignment is incorporated into the video diffusion model to improve temporal coherence and smoothness of the generated videos. *iii)* development of a medical video autoencoder incorporating frequency compensation to enhance the reconstruction quality of medical videos. Comprehensive experiments verify that our method *MedSora* establishes a new benchmark in state-of-the-art performance among existing medical video generation models, particularly in sustaining visual consistency and diminishing computational burden.

2 Preliminaries

2.1 Latent Diffusion Model

Latent Diffusion Models (LDM) (Rombach et al., 2022) are probabilistic denoising models that integrate autoencoders with predefined posterior distributions, rapidly becoming foundational components in the AIGC field. These models consist of two main processes: diffusion and denoising. During the diffusion process, random noise is progressively added to the latent representation \mathbf{z} through a sequence governed by a Markov chain with T -steps. Specifically, consider a fixed \mathbf{z} and a predetermined signal-noise schedule $\{\alpha_t, \sigma_t\}$, where the signal-to-noise ratio (SNR), given by (α_t^2/σ_t^2) , decreases monotonically as t increases. Define $\alpha_{t|s} = \alpha_t/\alpha_s$ and $\sigma_{t|s}^2 = \sigma_t^2 - \alpha_{t|s}^2\sigma_s^2$ for all $s < t$, we specify a series of latent variables \mathbf{z}_t for $t = 0, \dots, T$, which adhere to the following specified conditions:

$$q(\mathbf{z}_t|\mathbf{z}_s) = \begin{cases} \mathcal{N}(\mathbf{z}_t; \alpha_t\mathbf{z}_s, \sigma_t^2\mathbf{I}) & \text{if } s = 0 \\ \mathcal{N}(\mathbf{z}_t; \alpha_{t|s}\mathbf{z}_s, \sigma_{t|s}^2\mathbf{I}) & \text{if } s > 0 \end{cases}, \quad (1)$$

where \mathbf{I} represents the identity matrix. During the denoising phase, LDM train a reverse model $p_\theta(\mathbf{z}_s|\mathbf{z}_t)$, which reformulates a denoising objective,

$$p_\theta(\mathbf{z}_s|\mathbf{z}_t) = \mathcal{N}(\mathbf{z}_s; \mu_\theta(\mathbf{z}_t, \mathbf{c}, t), \Sigma_\theta(\mathbf{z}_t, \mathbf{c}, t)), \quad (2)$$

here \mathbf{c} represents the conditional input. The mean function μ_θ and the covariance matrix Σ_θ of the conditional distribution in the inverse process are calculated by training a denoising model ϵ_θ .

2.2 Scalar State-Space Models

The state space consists of a minimal set of variables that fully describe every possible state of the system. Building upon this concept, State-Space Models (SSM) (Gu et al., 2021a;b; Smith et al., 2022) define these variables to represent the system’s states and can predict future states based on specific inputs. To summarize, SSM defines a mapping from $\mathbf{x} \in \mathbb{R}^{(T,P)}$ to $\mathbf{y} \in \mathbb{R}^{(T,P)}$. The state transition is:

$$\mathbf{h}_t = \mathbf{A}_t\mathbf{h}_{t-1} + \mathbf{B}_t\mathbf{x}_t, \quad \mathbf{y}_t = \mathbf{C}_t^\top\mathbf{h}_t, \quad (3)$$

where $\mathbf{B}_t, \mathbf{C}_t \in \mathbb{R}^{(T,N)}$. \mathbf{h}_t is referred to as the hidden state, represented by an N -dimensional vector, where N is an independent hyperparameter, commonly referred to as the state dimension, state expansion factor, or state size. SSM are classified as regular (unstructured) SSM, diagonal (structured) SSM (Gu, 2023; Gupta et al., 2022), or scalar SSM (also known as SSD)(Dao & Gu, 2024), depending on whether the dimensions of \mathbf{A}_t are $\mathbb{R}^{(T,N,N)}$, $\mathbb{R}^{(T,N)}$, or $\mathbb{R}^{(T)}$, respectively. Selective SSM permit these parameters to change over time. Mamba(Gu & Dao, 2023), specifically its core

"S6" layer, exemplifies a selective SSM with diagonal structure. For computational efficiency, Eq.3 is implemented using matrix multiplication as follows:

$$\begin{aligned} \mathbf{y} &= \text{SSM}(\mathbf{A}, \mathbf{B}, \mathbf{C})(\mathbf{x}) = \mathbf{M}\mathbf{x}, \\ \text{s.t. } \mathbf{M}_{ij} &= \begin{cases} \mathbf{C}_i^\top \mathbf{A}_{i:j}^\mathbf{x} \mathbf{B}_j := \mathbf{C}_i^\top \mathbf{A}_i \cdots \mathbf{A}_{j+1} \mathbf{B}_j & \text{if } i \geq j \\ 0 & \text{if } i < j \end{cases}. \end{aligned} \quad (4)$$

Here \mathbf{M} is identified as a lower triangular semiseparable matrix. Mamba-2 (Dao & Gu, 2024) imposes a constraint that all diagonal elements of \mathbf{M} are identical, thereby restricting the diagonal to a scalar multiple of the identity matrix.

2.3 Optical Flow Estimation

The concept of optical flow (Zhai et al., 2021), originally introduced by Gibson (Gibson, 1950), represents a dense displacement vector field that describes the motion of pixels between consecutive frames under ideal conditions. Based on the displacement vector field (u, v) , the coordinates $(\mathbf{x}_x^k, \mathbf{x}_y^k)$ of each pixel in the k -th frame can be projected to the corresponding coordinates in the $(k+1)$ -th frame. In the $(k+1)$ -th frame, the new coordinates are determined by the coordinates in the k -th frame and the displacement vector field,

$$(\mathbf{x}_x^{k+1}, \mathbf{x}_y^{k+1}) = (\mathbf{x}_x^k + u^k(\mathbf{x}_x^k, \mathbf{x}_y^k), \mathbf{x}_y^k + v^k(\mathbf{x}_x^k, \mathbf{x}_y^k)). \quad (5)$$

Optical flow provides motion information that aids in understanding the dynamic and static regions within a moving scene. It accurately tracks the paths of objects in the video and effectively compensates for image instability caused by camera shaking or vibration, thereby ensuring smoother video presentation.

3 Methodology

Consider a dataset of videos \mathcal{D} , where each sample $\mathbf{x}^{1:F}$ is drawn from an unknown data distribution $p_{\text{data}}(\mathbf{x}^{1:F})$. In this context, each $\mathbf{x}^{1:F} := (\mathbf{x}^1, \dots, \mathbf{x}^F)$ corresponds to a sequence of video frames, with each frame sequence having a length $F > 1$ and a resolution of $H \times W$. Specifically, each frame $\mathbf{x}^\ell \in \mathbb{R}^{(C,H,W)}$, where C denotes the number of channels. The goal is to learn a model distribution $p_{\text{model}}(\mathbf{x}^{1:F})$ that precisely matches the original data distribution $p_{\text{data}}(\mathbf{x}^{1:F})$.

In the ensuing sections, we commence by detailing the architecture of diffusion model employed in *MedSora*, with a particular emphasis on components spatio Mamba and temporal Mamba (Section 3.1). Subsequently, we elucidate the implementation of the optical flow representation alignment (Section 3.2), followed by delving into the comprehensive fine-tuning strategy for the 3D causal VAE (Section 3.3). Finally, we provide a image and video joint training strategy (Section 3.4).

3.1 Video Mamba Diffusion Model

Current video diffusion models in the natural imaging typically employ either 3D or 2D+1D operations, simplifying the model excessively and thus compromising spatio-temporal performance. Alternatively, using standard self-attention mechanisms leads to significant computational overhead. In Figure 2, each block of our video diffusion framework consists of modules sequentially connected via spatial and temporal components. Considering Mamba’s limitations in local modeling and its proficiency in handling long sequences, and given the self-attention mechanism’s excellent local modeling capabilities but high computational cost that grows quadratically with sequence length, we propose employing local attention within the spatial component to model local information. To expand the receptive field to cover an entire video frame, we use Mamba to model long sequences along both the width and height axes, as shown in Figure 3. *The motivation for this is that both the width and height axes are high-dimensional, and correlations generally weaken with increasing distance, prompting us to selectively scan along these axes.*

Given a batch of video latent $\mathbf{z}^{1:f} \in \mathbb{R}^{(b,f,l,d)}$, derived from a batch of original videos $\mathbf{x}^{1:F} \in \mathbb{R}^{(B,F,C,H,W)}$ via a VAE, where l denotes the number of tokens in a sequence and d is the dimension of each token. The factorized local attention branch of the spatial component initially reshapes $\mathbf{z}^{1:f}$

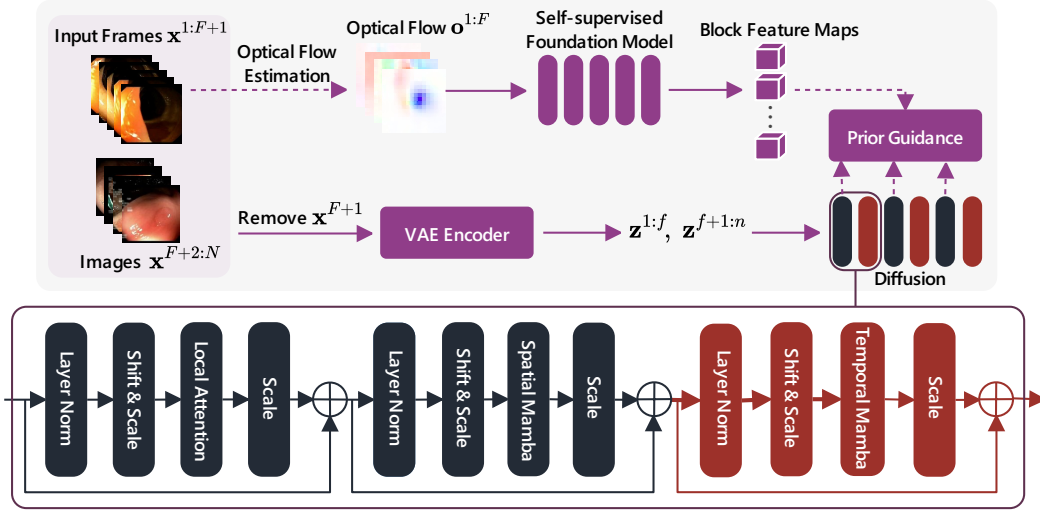


Figure 2: *MedSora* is built upon the video Mamba diffusion model, the optical flow representation alignment component, and the frequency compensation video VAE. The Video Mamba diffusion model enables video generation under low resource load; the optical flow representation alignment aims to produce smoother videos and accelerate model convergence; the frequency compensation video VAE addresses potential inconsistencies during the video reconstruction process.

into (bf, l, d) to facilitate spatial attention. For the i -th token in a sequence, define a sliding window $S(i)$ that encompasses the current position along with surrounding positions,

$$S(i) = \{j \mid j \in [\max(1, i - \lfloor \frac{w}{2} \rfloor), \min(f, i + \lfloor \frac{w}{2} \rfloor)]\}, \quad (6)$$

here w denotes the window size. The token at position i is then processed through multi-head attention with other tokens within the window to determine the output for that position,

$$\begin{aligned} \text{Scores}_{ij}^h &= \frac{\mathbf{Q}_i^h (\mathbf{K}_j^h)^\top}{\sqrt{d_k}}, \quad j \in S(i), \quad h \in \bar{H}, & \alpha_{ij}^h &= \frac{\exp(\text{Scores}_{ij}^h)}{\sum_{k \in S(i)} \exp(\text{Scores}_{ik}^h)}, \\ \text{Attention}_i^h &= \sum_{j \in S(i)} \alpha_{ij}^h \mathbf{V}_j^h, & \text{Attention}_i &= \text{Concat}(\text{Attention}_i^1, \dots, \text{Attention}_i^{\bar{H}}) \bar{W}_o, \end{aligned} \quad (7)$$

where \bar{H} is the number of heads in multi-head attention. $\mathbf{Q}^h = \mathbf{z}^{1:f} \bar{W}_q^h$, $\mathbf{K}^h = \mathbf{z}^{1:f} \bar{W}_k^h$, $\mathbf{V}^h = \mathbf{z}^{1:f} \bar{W}_v^h$, and each of \bar{W}_q^h , \bar{W}_k^h , \bar{W}_v^h , \bar{W}_o is a trainable weight matrix. We expand the input tensor $\mathbf{z}^{1:f}$ along the width and height axes to perform spatial Mamba in the shapes $(b\bar{h}, f\bar{w}, d)$ and $(b\bar{w}, f\bar{h}, d)$, respectively, where $\bar{w} = \bar{h} = \sqrt{l}$. To fuse the selective scanning results from these two directions, we integrate them using a gating mechanism.

As shown in Figure 3, prior to performing the selective scan with Mamba, the sequence of $f\bar{w}$ or $f\bar{h}$ tokens is rearranged according to the spiral direction and its reverse (denoted as Ω). Selective scan are then performed on both rearranged sequences. Subsequently, the original order of the results is restored using the spiral indexes, and the corresponding tokens at each position are summed (denoted as $\bar{\Omega}$). Without loss of generality, given an input tensor of shape (\hat{b}, \hat{l}, d) , where $\hat{b} = b\bar{h}$, $\hat{l} = f\bar{w}$ for height axis scanning or $\hat{b} = b\bar{w}$, $\hat{l} = f\bar{h}$ for width axis scanning. The spiral scanning process is

$$\begin{aligned} \{\mathbf{z}_1^{1:f}, \mathbf{z}_2^{1:f}, \dots, \mathbf{z}_l^{1:f}\} &\xrightarrow{\text{rearrange per } \Omega} \{\mathbf{z}_{\Omega_1}^{1:f}, \mathbf{z}_{\Omega_2}^{1:f}, \dots, \mathbf{z}_{\Omega_l}^{1:f}\}, \{\mathbf{z}_{\Omega_1}^{1:f}, \mathbf{z}_{\Omega_{l-1}}^{1:f}, \dots, \mathbf{z}_{\Omega_1}^{1:f}\}, \\ \{\bar{\mathbf{y}}_{\Omega_1}, \bar{\mathbf{y}}_{\Omega_2}, \dots, \bar{\mathbf{y}}_{\Omega_l}\} &= \text{SSM}(\mathbf{A}, \mathbf{B}, \mathbf{C})(\{\mathbf{z}_{\Omega_1}^{1:f}, \mathbf{z}_{\Omega_2}^{1:f}, \dots, \mathbf{z}_{\Omega_l}^{1:f}\}), \\ \{\hat{\mathbf{y}}_{\Omega_l}, \hat{\mathbf{y}}_{\Omega_{l-1}}, \dots, \hat{\mathbf{y}}_{\Omega_1}\} &= \text{SSM}(\mathbf{A}, \mathbf{B}, \mathbf{C})(\{\mathbf{z}_{\Omega_l}^{1:f}, \mathbf{z}_{\Omega_{l-1}}^{1:f}, \dots, \mathbf{z}_{\Omega_1}^{1:f}\}), \\ \{\bar{\mathbf{y}}_{\Omega_1}, \bar{\mathbf{y}}_{\Omega_2}, \dots, \bar{\mathbf{y}}_{\Omega_l}\}, \{\hat{\mathbf{y}}_{\Omega_l}, \hat{\mathbf{y}}_{\Omega_{l-1}}, \dots, \hat{\mathbf{y}}_{\Omega_1}\} &\xrightarrow{\text{rearrange per } \bar{\Omega}} \{\mathbf{y}_1, \mathbf{y}_2, \dots, \mathbf{y}_l\}. \end{aligned} \quad (8)$$

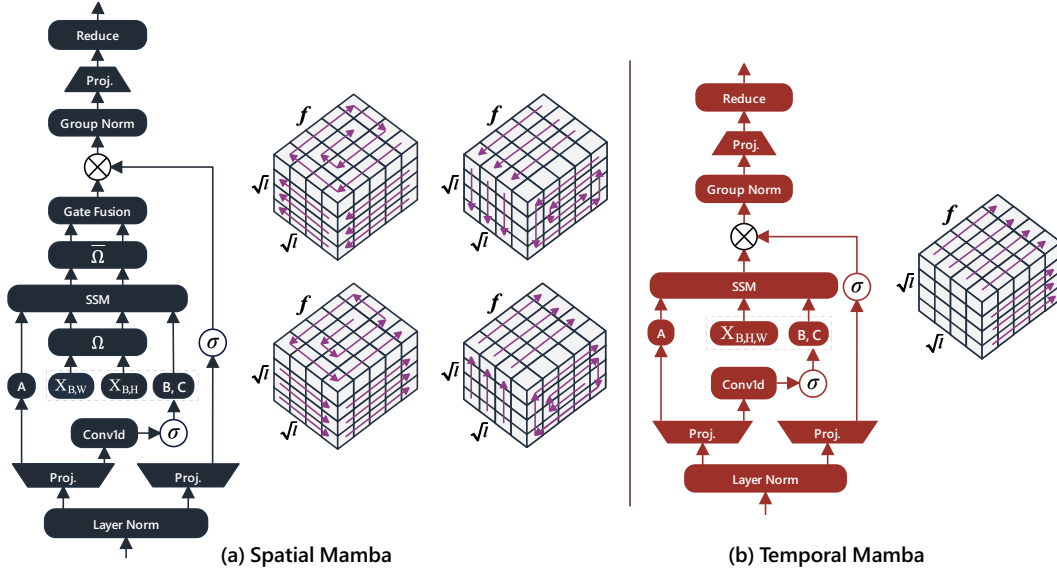


Figure 3: We present the structural details of spatial Mamba and temporal Mamba, both of which adopt the scalar state-space model. Spatial Mamba employ a bidirectional spiral scanning scheme to emphasize spatial continuity, while temporal Mamba scan along the frame axis.

Here $\mathbf{z}_i^{1:f} \in \mathbb{R}^{(\bar{b}, 1, d)}$ denotes the i -th token in the sequence. Following a spiral scan across both width and height dimensions, gated fusion is utilized to synthesize the outcomes from both axes,

$$\mathbf{y} = \sigma(W_1 \mathbf{y}_w + b_1) \odot \mathbf{y}_w + \sigma(W_2 \mathbf{y}_h + b_2) \odot \mathbf{y}_h, \quad (9)$$

where $\mathbf{y}_w := \{\mathbf{y}_1, \mathbf{y}_2, \dots, \mathbf{y}_{f\bar{w}}\}$ and $\mathbf{y}_h := \{\mathbf{y}_1, \mathbf{y}_2, \dots, \mathbf{y}_{f\bar{h}}\}$. σ is activation function. W_1, W_2, b_1 and b_2 are trainable parameters.

Following the modeling of individual video frames, we reshape the tensor $\mathbf{z}^{1:f}$ to shape (bl, f, d) and apply the temporal Mamba to selective scan along the frame axis, thereby extending the receptive field to encompass the entire video.

$$\{\mathbf{y}_1, \mathbf{y}_2, \dots, \mathbf{y}_f\} = \text{SSM}(\mathbf{A}, \mathbf{B}, \mathbf{C})(\{\mathbf{z}_1^{1:f}, \mathbf{z}_2^{1:f}, \dots, \mathbf{z}_f^{1:f}\}). \quad (10)$$

Computation Efficiency. For a video latent representation $\mathbf{z}^{1:f} \in \mathbb{R}^{(1, f, l, d)}$, the computational complexities of spatio-temporal self-attention and our method are as follows:

$$\begin{aligned} O(\text{Spatio-temporal self-attention}) &= \underbrace{f(4ld^2 + 2l^2d)}_{\text{spatial self-attention}} + \underbrace{l(4fd^2 + 2f^2d)}_{\text{temporal self-attention}} = 8fld^2 + 2fl^2d + 2lf^2d, \\ O(\text{Ours}) &= \underbrace{f(4ld^2 + 2lwd)}_{\text{local attention}} + \underbrace{2\bar{h}(3f\bar{w}(2d)\bar{N} + f\bar{w}(2d)\bar{N}^2) + 2\bar{w}(3f\bar{h}(2d)\bar{N} + f\bar{h}(2d)\bar{N}^2)}_{\text{spatial Mamba}} \\ &\quad + \underbrace{2l(2f(2d)\bar{N} + f(2d)\bar{N}^2)}_{\text{temporal Mamba}} = 4fld^2 + 2flwd + 18fld\bar{N} + 6fld\bar{N}^2. \end{aligned} \quad (11)$$

\bar{N} is a fixed parameter of Mamba, which is generally less than l . Eq.(11) demonstrates that the proposed video Mamba diffusion model significantly reduces the computational complexity.

3.2 Optical Flow Representation Alignment

Recent studies (Chen et al.; Xiang et al., 2023b; Li et al., 2023) have demonstrated that meaningful discriminative feature representations can be induced within diffusion models during the denoising process, achieved by implicitly learning the representation \mathbf{h} as the hidden state of a denoising

autoencoder that reconstructs the original data \mathbf{x} from its corrupted version. Compared to relying solely on the diffusion model to independently learn these representations, this method can enhance training efficiency and improve the quality of generation (Yu et al., 2024). This insight motivates us to enhance generative models by integrating external self-supervised representations. However, applying this approach to video generation presents challenges. First, the complex pixel movements between video frames are not fully considered. Most existing studies focus on image generation tasks, and the few that address video generation (Li et al., 2024) usually treat videos as sequences of individual images—inputting single-frame images into self-supervised models to obtain representations, and then integrating these representations. Second, there is an input mismatch problem: most self-supervised learning encoders are trained on clean images, whereas latent diffusion models typically use compressed latent representations from VAE with added noise as input. *To address these problems, we start by using a pre-trained optical flow prediction model RAFT (Teed & Deng, 2020) to track pixel motion across video frames, and employ a self-supervised visual model DINO (Caron et al., 2021) to extract motion feature representations. We then sample these motion feature representations and compute the covariance with the output of the spatial modeling from the video Mamba diffusion model, without requiring any additional parameter training.*

Optical flow estimation relies on analyzing consecutive frame pairs. To maintain consistency, we supply the optical flow prediction model with an extra frame, resulting in one more input frame than the VAE receives. Initially, the input $\mathbf{x}^{1:F+1}$ is processed using the optical flow prediction model RAFT to generate optical flow vector field $\mathbf{O}^{1:F}$. The i -th field encompasses the horizontal component \mathbf{O}_u^i and the vertical component \mathbf{O}_v^i , which define the vector transitions from the i -th frame to the $(i+1)$ -th frame and can be expressed as

$$\mathbf{O}_u^i = \begin{bmatrix} u^i(1,1) & u^i(1,2) & \cdots & u^i(1,W) \\ u^i(2,1) & u^i(2,2) & \cdots & u^i(2,W) \\ \vdots & \vdots & \ddots & \vdots \\ u^i(H,1) & u^i(H,2) & \cdots & u^i(H,W) \end{bmatrix}, \mathbf{O}_v^i = \begin{bmatrix} v^i(1,1) & v^i(1,2) & \cdots & v^i(1,W) \\ v^i(2,1) & v^i(2,2) & \cdots & v^i(2,W) \\ \vdots & \vdots & \ddots & \vdots \\ v^i(H,1) & v^i(H,2) & \cdots & v^i(H,W) \end{bmatrix}. \quad (12)$$

Since the self-supervised foundation model DINO accepts a three-dimensional RGB image as input, the two-dimensional optical flow field must be further processed. Specifically, for the horizontal component $u^i(x, y)$ and vertical component $v^i(x, y)$ at position (x, y) in the i -th optical flow field, we encode the two-dimensional optical flow vector into an RGB pixel. This representation not only intuitively illustrates the direction of motion but also effectively conveys the intensity of motion. Mathematically,

$$\begin{aligned} M^i(x, y) &= \sqrt{u^i(x, y)^2 + v^i(x, y)^2}, & A^i(x, y) &= \arctan\left(\frac{v^i(x, y)}{u^i(x, y)}\right), \\ H^i(x, y) &= \frac{A^i(x, y)}{2\pi} \times 360^\circ, & S^i(x, y) &= 1, & V^i(x, y) &= \frac{M^i(x, y)}{M_{\max}^i}, \\ (R^i(x, y), G^i(x, y), B^i(x, y)) &= \text{HSVtoRGB}(H^i(x, y), S^i(x, y), V^i(x, y)). \end{aligned} \quad (13)$$

Eq.(13) initially represents $u^i(x, y)$ and $v^i(x, y)$ in terms of motion intensity $M^i(x, y)$ and direction $A^i(x, y)$. Subsequently, these components are mapped to the HSV color space, where $H^i(x, y)$, $S^i(x, y)$, $V^i(x, y)$ respectively denote hue, saturation, and value. Finally, the HSV pixel is converted to an RGB pixel using a standard color space conversion method.

We employ the self-supervised foundation model DINO, which exhibits high semantic relevance, to extract dense features from optical flow images. Specifically, the optical flow image derived from Eq.(13) is fed into the DINO model to yield multi-scale representations that span from shallow to deep layers, denoted as $[\mathbf{h}_1^*, \mathbf{h}_2^*, \dots, \mathbf{h}_D^*]$. These representations are then aligned with the reshaped output features $[\mathbf{y}_1^*, \mathbf{y}_2^*, \dots, \mathbf{y}_L^*]$ of the spatial component. Here $\mathbf{h}_i^* \in \mathbb{R}^{(\tilde{N}, \tilde{K})}$, $\mathbf{y}_i^* \in \mathbb{R}^{(K, d)}$, $\tilde{K} = bF\tilde{l}$, $K = bfl$ and \tilde{l} is the sequence length of DINO. We utilize the relative distribution similarity (Tang et al., 2024) to match features,

$$\begin{aligned} \mathbf{r}_{i,d_i}^{1:f} &:= 1 - \frac{\sum_{k=1}^K (\mathbf{y}_{i,k,d_i}^* - \bar{\mathbf{y}}_{i,d_i}^*) (\text{Sampling}(\mathbf{h}_{\nu_i,k,d_i}^*) - \bar{\mathbf{h}}_{\nu_i,d_i}^*)}{\sqrt{\sum_{k=1}^K (\mathbf{y}_{i,k,d_i}^* - \bar{\mathbf{y}}_{i,d_i}^*)^2} \sqrt{\sum_{k=1}^K (\text{Sampling}(\mathbf{h}_{\nu_i,k,d_i}^*) - \bar{\mathbf{h}}_{\nu_i,d_i}^*)^2}}, \quad i \in L, d_i \in d, \\ \text{where } \bar{\mathbf{h}}_{\nu_i,d_i}^* &= \frac{1}{K} \sum_{k=1}^K \text{Sampling}(\mathbf{h}_{\nu_i,k,d_i}^*), \quad \bar{\mathbf{y}}_{i,d_i}^* = \frac{1}{K} \sum_{k=1}^K \mathbf{y}_{i,k,d_i}^*. \end{aligned} \quad (14)$$

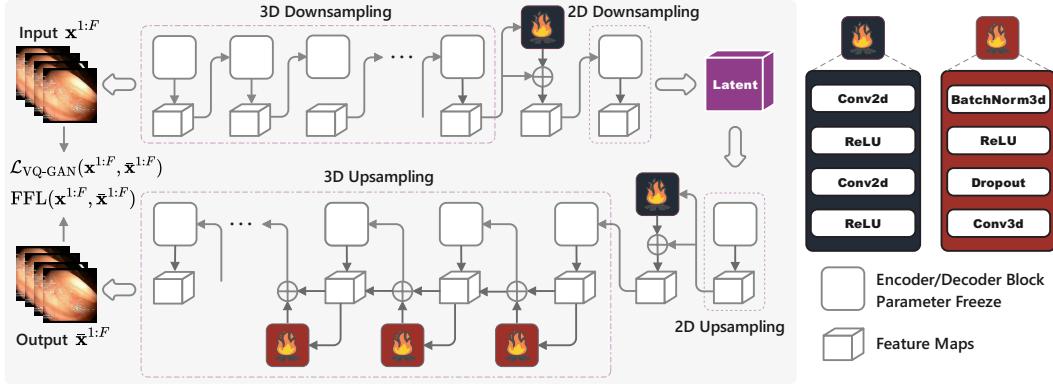


Figure 4: The proposed frequency compensation video VAE. Current video diffusion models either rely on image VAEs for encoding and reconstructing videos, potentially omitting crucial temporal information and resulting in inadequate compression rates, or rely on video VAEs that lack training on medical videos. The proposed frequency compensation video VAE introduces frequency compensation components with two distinct structures, built on the 3D causal VAE, ensuring temporal consistency while focusing on the structural information of medical videos, which is instrumental in identifying areas such as lesions and textures.

We use $\mathbf{h}_{\nu_i}^*$ represents the optical flow representation corresponding to \mathbf{y}_i^* , which is selected from the set $[\mathbf{h}_1^*, \mathbf{h}_2^*, \dots, \mathbf{h}_D^*]$. $\text{Sampling}(\cdot)$ denotes the application of bilinear interpolation to the first dimension of $\mathbf{h}_{\nu_i}^*$ and 1×1 convolution to its second dimension, ensuring that $\mathbf{h}_{\nu_i}^*$ and \mathbf{y}_i^* have consistent dimensions. We define the optical flow representation alignment loss as follows:

$$\mathcal{L}_{\text{Align}}^{1:f} = \max\left(\frac{1}{Ld} \sum_{i=1}^L \sum_{d_i=1}^d g(t) \cdot \mathbf{r}_{i,d_i}^{1:f} - \text{margin}, 0\right). \quad (15)$$

$t \in [0, T)$ signifies the time step or stage index, and T represents the predetermined total number of steps. As t progresses, the noise superimposed on the video latent intensifies, consequently diminishing the discriminative representational capacity of the output features from the diffusion model’s spatial components. In response, we propose introducing a hyperparameter $g(t)$, which is inversely proportional to t , to regulate the variable $\mathbf{r}_{i,d_i}^{1:f}$, set to $1/(t+1)$ by default. Furthermore, we incorporate a hyperparameter margin in Eq.(15) for regularization purposes, aiming to enhance the separation or decorrelation among features. By neglecting small $\mathbf{r}_{i,d_i}^{1:f}$, we prevent the model from overemphasizing minor differences, thereby steering the training process towards correcting more substantial errors and enhancing the model’s robustness.

3.3 Frequency Compensation Video VAE

Many video diffusion models employ image VAEs to compress source videos into latent space and then reconstruct the videos within that space (Wu et al., 2023; Chen et al., 2023b; Xing et al., 2024b). However, since videos encapsulate both spatial and temporal information, the absence of temporal components in image VAEs precludes capturing inter-frame dependencies, often resulting in artifacts, flickering, or temporal inconsistencies (Blattmann et al., 2023; Xiang et al., 2023a). Furthermore, given that video data significantly exceeds image data in size, and image VAEs solely compress spatial dimensions, they fail to efficiently compress along the temporal dimension, resulting in relatively large latent representations for videos.

Recent works have implemented 3D VAEs video compression module by employing 3D convolutions to compress both the temporal and spatial dimensions of videos (Yang et al., 2024). However, the scarcity of medical video datasets often hinders these VAEs from being adequately trained, leading to insufficient generalization in medical field.

To effectively adapt to the medical video generation task, and in light of the significant advantages of frequency methods in processing medical data with complex structural features, we introduced frequency compensation modules into the 3D causal VAE (Yang et al., 2024). During the training phase, in addition to employing the same optimization loss as VQ-GAN (Esser et al., 2021), we also introduced the Focal Frequency Loss (Jiang et al., 2021) to narrow the gap between the original and generated videos in the frequency domain, thereby more accurately capturing structural information such as the edge and texture features of the lesion. To optimize training efficiency, we freeze the original parameters of the 3D causal VAE and insert the frequency compensation modules before the encoder’s 2D downsampling block and in the middle of each decoder block. As shown in Figure 4.

The frequency compensation modules contain two components with different structures. The component close to the 2D sampling blocks uses standard 2D convolution to reconstruct space, and the other component uses standard 3D convolution to reconstruct time and space. The final optimization loss for fine-tuning the 3D causal VAE is formulated as follows:

$$\mathcal{L}_{\text{VAE}} = \mathcal{L}_{\text{VQ-GAN}}(\mathbf{x}^{1:F}, \bar{\mathbf{x}}^{1:F}) + \lambda \text{FFL}(\mathbf{x}^{1:F}, \bar{\mathbf{x}}^{1:F}). \quad (16)$$

$\mathcal{L}_{\text{VQ-GAN}}(\cdot, \cdot)$ is the reconstruction loss as in VQ-GAN, includes L1 loss and perceptual similarity loss (Zhang et al., 2018), λ is a weight coefficient, set to 0.1 by default.

3.4 Image and Video Joint Training

Several studies have demonstrated that the joint training of videos and images significantly improves the quality and diversity of video generation (Ho et al., 2022; Gupta et al., 2023; Wang et al., 2023) while mitigating the phenomenon of forgetting (Chen et al., 2023a). To implement this joint training, we randomly select independent images $\mathbf{x}^{F+2:N}$ from various videos within the same dataset and concatenate them to the end of each video $\mathbf{x}^{1:F}$ sampled randomly from the dataset. The training loss for the video Mamba diffusion model is

$$\begin{aligned} \mathcal{L}_{\text{DDPM}} &= \|\epsilon - \epsilon_{\theta}(\mathbf{z}_t^{1:f}, \mathbf{z}_t^{f+1:n}, t)\|^2 + \alpha \mathcal{L}_{\text{Align}}^{1:f}, \\ \text{s.t. } t &\in [0, T), \mathbf{z}_t^{1:f} \sim q(\mathbf{z}_t^{1:f} | \mathbf{z}_s^{1:f}), \mathbf{z}_t^{f+1:n} \sim q(\mathbf{z}_t^{f+1:n} | \mathbf{z}_s^{f+1:n}), \epsilon \sim \mathcal{N}(0, \mathbf{I}), \end{aligned} \quad (17)$$

where α is a hyperparameter. We mask the images when computing $\mathcal{L}_{\text{Align}}^{1:f}$ to prevent the introduction of spurious optical flow motion trajectories between individual images.

4 Experiments

4.1 Implementation Details

Video Mamba diffusion model was trained using the AdamW optimizer (Loshchilov, 2017), which employs a phased learning rate adjustment strategy. During the initial 2 epochs, a learning rate of 1×10^{-3} and a batch size of 16 was used to accelerate convergence. Subsequently, the learning rate was fixed at 1×10^{-4} and the batch size was set to 2 to achieve more stable and fine-grained parameter optimization. In alignment with the settings of the sole existing medical video generation work (Li et al., 2024), we configured the training video to consist of 16 frames, each with a resolution of 128×128 pixels. In addition, we randomly selected 8 images for joint training, each matching the resolution of the video frame. Data augmentation was performed solely through horizontal flipping. Consistent with standard practices in diffusive generative models, we did not modify the decay/warm-up schedule, learning rate, or Adam β_1/β_2 hyperparameters. Training incorporated the exponential moving average (EMA) (Tarvainen & Valpola, 2017; Wang et al., 2022) with a decay rate of 0.9999. The performance outcomes of the EMA model were reported for final result sampling. Each dataset undergoes training for one week using early stopping strategy to prevent overfitting, in line with standard practices for video-related tasks. Gradient clipping is initiated at the 25-th epoch, with the clip max norm set to 1.0 to ensure training stability. Unless otherwise specified, the hyperparameter α is set to 0.01. Most of our experiments utilized multiple Nvidia RTX 3090 Ti GPUs. During the inference stage, videos are generated via DDIM sampling (Song et al., 2020). Additional training details and network specifications are outlined in Table 1.

During the training of the frequency compensation video VAE, we utilize the Adam optimizer, conducting training across each dataset for 10 epochs, setting the learning rate to 2×10^{-7} , and configuring the momentum parameters β_1 and β_2 to 0.5 and 0.9, respectively.

Table 1: *MedSora* network detail. We introduce three variants of our model, distinguished by network depth, selected DINO layer features, and parameter count. The depth and patch size can be adjusted to scale the network as desired. Notably, our model has significantly fewer parameters compared to existing video generation models of same depth and patch size.

| | MedSora-S | MedSora-B | MedSora-L |
|-----------------------------------|-------------------------------------|--------------------------------------|--------------------------------------|
| Architecture | LDM | LDM | LDM |
| video resolution | $16 \times 128 \times 128 \times 3$ | $16 \times 128 \times 128 \times 3$ | $16 \times 128 \times 128 \times 3$ |
| images resolution | $8 \times 128 \times 128 \times 3$ | $8 \times 128 \times 128 \times 3$ | $8 \times 128 \times 128 \times 3$ |
| z-shape | $6 \times 16 \times 16 \times 16$ | $6 \times 16 \times 16 \times 16$ | $6 \times 16 \times 16 \times 16$ |
| Embedding dimension | 512 | 512 | 512 |
| Depth | 6 | 12 | 24 |
| Patch size | 2 | 2 | 2 |
| Strip size | 2 | 2 | 2 |
| Local attention | | | |
| Window size | 8 | 8 | 8 |
| Look backward | 1 | 1 | 1 |
| Look forward | 1 | 1 | 1 |
| Dropout | 0.1 | 0.1 | 0.1 |
| Exact window size | True | True | True |
| Spatial&Temporal Mamba | | | |
| State expansion factor | 128 | 128 | 128 |
| Local convolution width | 4 | 4 | 4 |
| Expand | 2 | 2 | 2 |
| Head dimension | 64 | 64 | 64 |
| A init range | (1, 16) | (1, 16) | (1, 16) |
| Groups norm | 1 | 1 | 1 |
| Δ min | 0.001 | 0.001 | 0.001 |
| Δ max | 0.1 | 0.1 | 0.1 |
| Δ init floor | 1×10^{-4} | 1×10^{-4} | 1×10^{-4} |
| Chunk size | 256 | 256 | 256 |
| Optical flow sampling | | | |
| Selected DINO Layers | [0, 2, 4, 6, 8, 10] | $0 \rightarrow 11$ | $0, 0 \rightarrow 11, 11$ |
| Bilinear interpolation size | (64, 512) | (64, 512) | (64, 512) |
| Convolution | $(1 \times 1, 16 \rightarrow 4)$ | $(1 \times 1, 16 \rightarrow 4)$ | $(1 \times 1, 16 \rightarrow 4)$ |
| Training | | | |
| Parameterization | ϵ | ϵ | ϵ |
| Learning rate | - | $1 \times 10^{-3}, 1 \times 10^{-4}$ | $1 \times 10^{-3}, 1 \times 10^{-4}$ |
| Batch size | - | 16, 2 | 16, 2 |
| Start gradient clipping | - | 25 epoch | 25 epoch |
| Clip max norm | - | 1 | 1 |
| Diffusion steps | - | 1000 | 1000 |
| Noise schedule | Linear | Linear | Linear |
| Sampling | | | |
| Sampler | DDIM | DDIM | DDIM |
| Steps | 250 | 250 | 250 |
| Total training parameters | 43.76 M | 86.47 M | 171.89 M |

4.2 Dataset Setting

Colonoscopic (Mesejo et al., 2016). The Colonoscopic dataset comprises 210 colonoscopy videos, each annotated by medical experts to identify various types of lesions including polyps, cancers, and other non-malignant formations. Each video ranges from 30 seconds to one minute in duration and includes 30 frames per second, with each frame having a resolution of 768×576 pixels.

CholecTriplet (Nwoye et al., 2022). The CholecTriplet dataset is an endoscopic video dataset that extends the CholecT40 dataset (Nwoye et al., 2020) for laparoscopic cholecystectomy surgery, annotated with triple information in the format $\langle \text{instrument, verb, target} \rangle$. The dataset comprises 50 videos, including 45 from the Cholec80 dataset (Twinanda et al., 2016) and 5 from an internal dataset of the same surgical procedure.

Kvasir-Capsul (Borgli et al., 2020). The Kvasir-Capsule dataset comprises 117 videos, each annotated at the frame level. These videos were captured using capsule endoscope, a small swallowable camera device that can capture detailed videos of the gastrointestinal tract, particularly the small intestine. The dataset includes annotated videos across various gastrointestinal conditions, including normal findings and common illnesses, providing a valuable resource for the research and development of automated lesion detection algorithms.

We extracted 16 frame video clips from these datasets *by sampling every third frame*, and resized each frame to 128×128 for training.

4.3 Evaluation

We assessed *MedSora* employing five metrics: Fréchet Video Distance (FVD) (Unterthiner et al., 2018); Content-Debiased Fréchet Video Distance (CD-FVD) (Ge et al., 2024), which is an enhanced version of the FVD, offering superior accuracy in measuring actual motion; Fréchet Inception Distance (FID) (Heusel et al., 2017); Inception Score (IS) (Saito et al., 2017). And in our analysis study, we additionally used Frame Consistency (FC) to evaluate video continuity by computing the mean CLIP similarity between consecutive frames (Esser et al., 2023). Following the evaluation criteria outlined in StyleGAN-V (Skorokhodov et al., 2022), we used 2048 video clips to calculate the metrics.

4.4 Quantitative Evaluation

We compare our method *MedSora* with four publicly available video generation methods: StyleGAN-V (Skorokhodov et al., 2022), MoStGAN-V (Shen et al., 2023), LVDM (He et al., 2022), and Endora (Li et al., 2024). As presented in Table 2, *MedSora* outperforms the state-of-the-art GAN-based methods StyleGAN-V and MoStGAN-V across all performance metrics. Furthermore, *MedSora* surpasses the diffusion-based methods LVDM and Endora (base size) while utilizing fewer training parameters.

Table 2: Quantitative comparisons between *MedSora* and other video generation methods.

| | Colonoscopic | | | | CholecTriplet | | | | Kvasir-Capsul | | | |
|------------|--------------|---------|--------|------|---------------|---------|--------|------|---------------|---------|--------|------|
| | FVD↓ | CD-FVD↓ | FID↓ | IS↑ | FVD↓ | CD-FVD↓ | FID↓ | IS↑ | FVD↓ | CD-FVD↓ | FID↓ | IS↑ |
| StyleGAN-V | 1994.1 | 630.87 | 226.59 | 1.95 | 648.37 | 747.35 | 86.26 | 3.37 | 183.82 | 854.42 | 29.99 | 2.76 |
| LVDM | 1271.2 | 620.41 | 97.56 | 1.91 | 1007.9 | 1314.0 | 109.02 | 3.20 | 1013.6 | 750.62 | 196.35 | 1.45 |
| MoStGAN-V | 437.96 | 332.93 | 53.42 | 3.31 | 446.17 | 461.18 | 72.61 | 3.56 | 89.74 | 89.11 | 15.52 | 2.53 |
| Endora | 468.37 | 393.19 | 13.75 | 3.86 | 383.88 | 575.53 | 30.02 | 3.58 | 114.36 | 96.68 | 18.33 | 2.31 |
| MedSora-B | 462.04 | 332.23 | 15.47 | 3.88 | 447.78 | 447.69 | 24.98 | 3.63 | 92.36 | 86.43 | 12.06 | 2.38 |
| MedSora-L | 429.35 | 310.58 | 13.42 | 3.93 | 400.60 | 412.52 | 20.02 | 3.98 | 76.71 | 80.50 | 10.48 | 2.44 |

4.5 Qualitative Evaluation

Figure 5 further demonstrates the qualitative results of *MedSora* alongside comparison methods. We observed that other video generation techniques exhibit the following issues: *i*) video distortion (StyleGAN), *ii*) overly consistent frames with insufficient dynamic representation (MoStGAN and LVDM), *iii*) abnormal video imagery that conflicts with anatomical structures (LVDM), and *iv*) video frames display artifacts or blurring, the transitions between frames lack coherence (Endora). In contrast, the video frames generated by *MedSora* avoid inconsistent visual distortions, and the transitions between frames are coherent, exhibiting high visual quality and dynamic expression.

Furthermore, *MedSora* maintains color consistency and detail clarity, rendering the generated video more visually realistic.

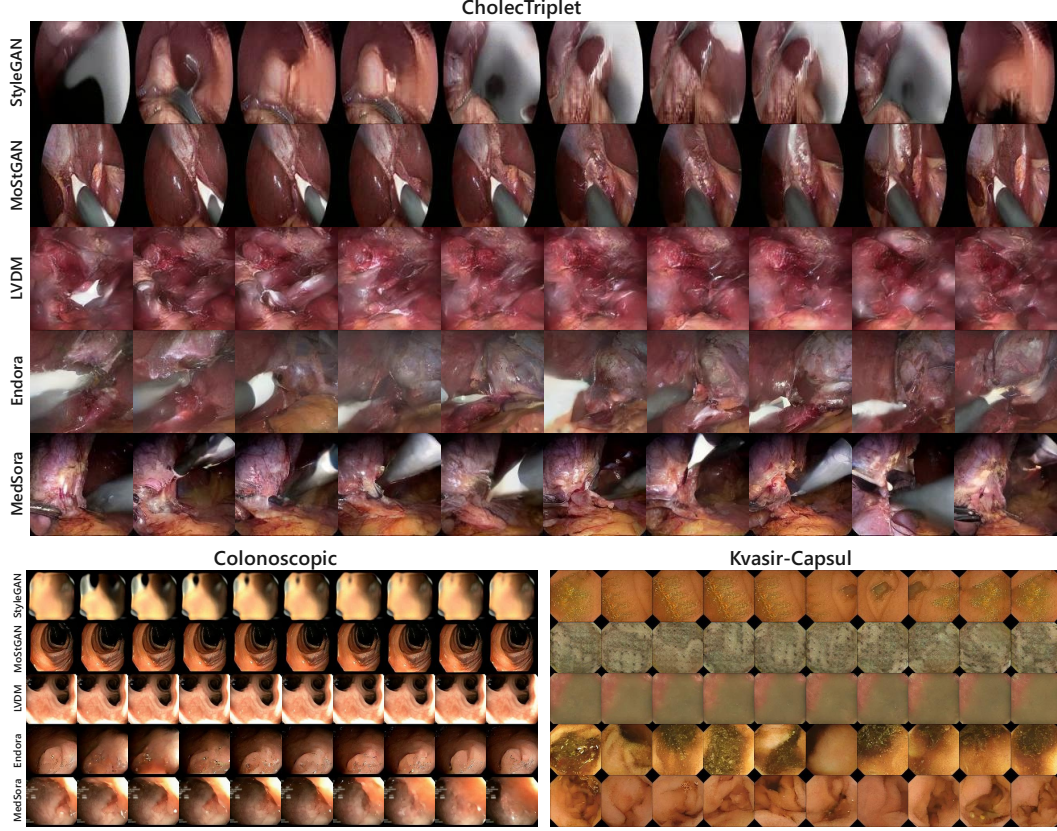


Figure 5: Qualitative comparison between *MedSora* and other video generation models. The generated videos consist of 16 frames, from which 10 consecutive frames starting at $t = 0$ are selected for demonstration. For a more comprehensive comparison of qualitative results, please refer to the generated videos on our project webpage.

To demonstrate that videos generated by *MedSora* exhibit greater stability and smoother frame transitions than Endora, we computed the FC scores between consecutive frames of videos generated by both models. As presented in Table 3, the results indicate that *MedSora* consistently achieves higher FC scores than Endora across the three datasets, confirming its superior frame consistency.

Table 3: Comparison of FC scores between *MedSora* and Endora.

| Method | Colonoscopic | CholeTriplet | Kvasir-Capsul |
|-----------|--------------|--------------|---------------|
| Endora | 95.43 | 91.15 | 90.70 |
| MedSora-B | 97.17 | 94.19 | 94.02 |

4.6 Training Efficiency

Figure 6 summarizes the floating-point operations (FLOPs), parameter size, and memory consumption involved in training the video Mamba diffusion model, and compare with Endora (base size), a method tailored for medical video generation tasks. As shown in Figure 6, *MedSora-B* outperforms Endora even though it uses fewer parameters and less memory. This superior performance is due to our proposed optical flow representation alignment supervision and frequency compensation

video VAE, which effectively capture the spatio-temporal information of the video. In addition, we observed that although *MedSora-L* has slightly more parameters than Endora, its FLOPs are significantly lower. This is because the use of frequency compensation video VAE enables a higher compression rate than the previous image VAEs, and the carefully designed spatio-temporal Mamba structure avoids the quadratic computational complexity introduced by global self-attention.

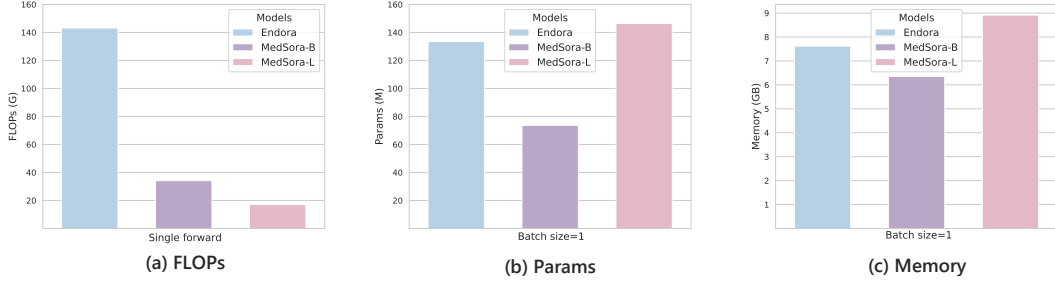


Figure 6: Comparison of training efficiency. (a) FLOPs, (b) model parameter scale, and (c) memory (GB) of different methods that are trained on 16 frame videos with resolution of 128×128 and batch size of 1. To ensure a fair comparison, we do not apply gradient checkpointing to any of the models.

4.7 An Example of Downstream Task

We investigated the utilization of video generation models in downstream semi-supervised tasks. Specifically, within the PolyDiag (Tian et al., 2022) training set, we randomly selected 40 videos as labeled data and generated 200 additional videos as unlabeled data to train a disease classification model. Table 4 presents the F1 scores of the classification model on the Colonoscopic and CholecTriplet datasets. The results indicate that employing generated videos for semi-supervised training substantially enhances the performance. Furthermore, In addition, compared to fake videos produced by other video generation methods, those generated by *MedSora* demonstrated superior downstream performance. The result indicates that the videos generated by *MedSora* are more realistic, thereby validating *MedSora*’s effectiveness as a medical video simulator.

Table 4: Semi-supervised classification F1 score on PolyDiag.

| Method | Colonoscopic | CholeTriplet |
|-----------------|----------------|---------------|
| Supervised-only | 74.26 | 74.70 |
| LVDM | 75.92 (+1.66) | 77.88 (+3.18) |
| Endora | 86.73 (+12.47) | 81.89 (+7.19) |
| MedSora-B | 88.12 (+13.86) | 83.01 (+8.31) |

5 Conclusion

This paper introduces *MedSora*, an exploratory framework for medical video generation. Specifically, by considering the advantages and disadvantages of attention and Mamba, we propose a video Mamba diffusion model framework that efficiently models the spatio-temporal information in medical videos. To accurately capture inter-frame pixel motion, we propose optical flow representation alignment to assist in the training of the diffusion model. Additionally, we enhance the 3D causal VAE for efficient compression of medical videos. In benchmark experiments on medical video datasets, *MedSora* demonstrated excellent performance across various metrics, computational efficiency, and impressive potential as a medical video simulator for downstream tasks. We anticipate that this work will inspire further research in medical video generation and contribute significant breakthroughs to generative AI in medicine.

References

- Jie An, Songyang Zhang, Harry Yang, Sonal Gupta, Jia-Bin Huang, Jiebo Luo, and Xi Yin. Latent-shift: Latent diffusion with temporal shift for efficient text-to-video generation. arXiv preprint arXiv:2304.08477, 2023.
- Andreas Blattmann, Robin Rombach, Huan Ling, Tim Dockhorn, Seung Wook Kim, Sanja Fidler, and Karsten Kreis. Align your latents: High-resolution video synthesis with latent diffusion models. In Proceedings of the IEEE/CVF Conference on Computer Vision and Pattern Recognition, pp. 22563–22575, 2023.
- Hanna Borgli, Vajira Thambawita, Pia H Smedsrud, Steven Hicks, Debesh Jha, Sigrun L Eskeland, Kristin Ranheim Randel, Konstantin Pogorelov, Mathias Lux, Duc Tien Dang Nguyen, et al. Hyperkvasir, a comprehensive multi-class image and video dataset for gastrointestinal endoscopy. Scientific data, 7(1):283, 2020.
- Tom Brown, Benjamin Mann, Nick Ryder, Melanie Subbiah, Jared D Kaplan, Prafulla Dhariwal, Arvind Neelakantan, Pranav Shyam, Girish Sastry, Amanda Askell, et al. Language models are few-shot learners. Advances in neural information processing systems, 33:1877–1901, 2020.
- Mathilde Caron, Hugo Touvron, Ishan Misra, Hervé Jégou, Julien Mairal, Piotr Bojanowski, and Armand Joulin. Emerging properties in self-supervised vision transformers. In Proceedings of the IEEE/CVF international conference on computer vision, pp. 9650–9660, 2021.
- Haoxin Chen, Menghan Xia, Yingqing He, Yong Zhang, Xiaodong Cun, Shaoshu Yang, Jinbo Xing, Yaofang Liu, Qifeng Chen, Xintao Wang, et al. Videocrafter1: Open diffusion models for high-quality video generation. arXiv preprint arXiv:2310.19512, 2023a.
- Weifeng Chen, Yatai Ji, Jie Wu, Hefeng Wu, Pan Xie, Jiashi Li, Xin Xia, Xuefeng Xiao, and Liang Lin. Control-a-video: Controllable text-to-video generation with diffusion models. arXiv preprint arXiv:2305.13840, 2023b.
- X Chen, Z Liu, S Xie, and K He. Deconstructing denoising diffusion models for self-supervised learning. arxiv 2024. arXiv preprint arXiv:2401.14404.
- Tri Dao and Albert Gu. Transformers are ssms: Generalized models and efficient algorithms through structured state space duality. arXiv preprint arXiv:2405.21060, 2024.
- Ali Diba, Vivek Sharma, Mohammad Arzani, Luc Van Gool, et al. Spatio-temporal convolution-attention video network. In Proceedings of the IEEE/CVF International Conference on Computer Vision, pp. 859–869, 2023.
- Patrick Esser, Robin Rombach, and Bjorn Ommer. Taming transformers for high-resolution image synthesis. In Proceedings of the IEEE/CVF conference on computer vision and pattern recognition, pp. 12873–12883, 2021.
- Patrick Esser, Johnathan Chiu, Parmida Atighehchian, Jonathan Granskog, and Anastasis Germanidis. Structure and content-guided video synthesis with diffusion models. In Proceedings of the IEEE/CVF International Conference on Computer Vision, pp. 7346–7356, 2023.
- David Fleet and Yair Weiss. Optical flow estimation. In Handbook of mathematical models in computer vision, pp. 237–257. Springer, 2006.
- Yu Gao, Jiancheng Huang, Xiaopeng Sun, Zequn Jie, Yujie Zhong, and Lin Ma. Matten: Video generation with mamba-attention. arXiv preprint arXiv:2405.03025, 2024.
- Songwei Ge, Aniruddha Mahapatra, Gaurav Parmar, Jun-Yan Zhu, and Jia-Bin Huang. On the content bias in fréchet video distance. In Proceedings of the IEEE/CVF Conference on Computer Vision and Pattern Recognition (CVPR), 2024.
- James J Gibson. The perception of the visual world. 1950.
- Ian Goodfellow, Jean Pouget-Abadie, Mehdi Mirza, Bing Xu, David Warde-Farley, Sherjil Ozair, Aaron Courville, and Yoshua Bengio. Generative adversarial nets. Advances in neural information processing systems, 27, 2014.

- Albert Gu. Modeling Sequences with Structured State Spaces. Stanford University, 2023.
- Albert Gu and Tri Dao. Mamba: Linear-time sequence modeling with selective state spaces. arXiv preprint arXiv:2312.00752, 2023.
- Albert Gu, Karan Goel, and Christopher Ré. Efficiently modeling long sequences with structured state spaces. arXiv preprint arXiv:2111.00396, 2021a.
- Albert Gu, Isys Johnson, Karan Goel, Khaled Saab, Tri Dao, Atri Rudra, and Christopher Ré. Combining recurrent, convolutional, and continuous-time models with linear state space layers. Advances in neural information processing systems, 34:572–585, 2021b.
- Agrim Gupta, Lijun Yu, Kihyuk Sohn, Xiuye Gu, Meera Hahn, Li Fei-Fei, Irfan Essa, Lu Jiang, and José Lezama. Photorealistic video generation with diffusion models. arXiv preprint arXiv:2312.06662, 2023.
- Ankit Gupta, Albert Gu, and Jonathan Berant. Diagonal state spaces are as effective as structured state spaces. Advances in Neural Information Processing Systems, 35:22982–22994, 2022.
- Yingqing He, Tianyu Yang, Yong Zhang, Ying Shan, and Qifeng Chen. Latent video diffusion models for high-fidelity long video generation. arXiv preprint arXiv:2211.13221, 2022.
- Martin Heusel, Hubert Ramsauer, Thomas Unterthiner, Bernhard Nessler, and Sepp Hochreiter. Gans trained by a two time-scale update rule converge to a local nash equilibrium. Advances in neural information processing systems, 30, 2017.
- Jonathan Ho, Ajay Jain, and Pieter Abbeel. Denoising diffusion probabilistic models. Advances in neural information processing systems, 33:6840–6851, 2020.
- Jonathan Ho, Tim Salimans, Alexey Gritsenko, William Chan, Mohammad Norouzi, and David J Fleet. Video diffusion models. Advances in Neural Information Processing Systems, 35:8633–8646, 2022.
- Edward J Hu, Yelong Shen, Phillip Wallis, Zeyuan Allen-Zhu, Yanzhi Li, Shean Wang, Lu Wang, and Weizhu Chen. Lora: Low-rank adaptation of large language models. arXiv preprint arXiv:2106.09685, 2021.
- Hanzhuo Huang, Yufan Feng, Cheng Shi, Lan Xu, Jingyi Yu, and Sibe Yang. Free-bloom: Zero-shot text-to-video generator with llm director and ldm animator. Advances in Neural Information Processing Systems, 36, 2024.
- Liming Jiang, Bo Dai, Wayne Wu, and Chen Change Loy. Focal frequency loss for image reconstruction and synthesis. In Proceedings of the IEEE/CVF international conference on computer vision, pp. 13919–13929, 2021.
- Levon Khachatryan, Andranik Movsisyan, Vahram Tadevosyan, Roberto Henschel, Zhangyang Wang, Shant Navasardyan, and Humphrey Shi. Text2video-zero: Text-to-image diffusion models are zero-shot video generators. In Proceedings of the IEEE/CVF International Conference on Computer Vision, pp. 15954–15964, 2023.
- Diederik P Kingma and Max Welling. Auto-encoding variational bayes. arXiv preprint arXiv:1312.6114, 2013.
- Alexander C Li, Mihir Prabhudesai, Shivam Duggal, Ellis Brown, and Deepak Pathak. Your diffusion model is secretly a zero-shot classifier. In Proceedings of the IEEE/CVF International Conference on Computer Vision, pp. 2206–2217, 2023.
- Chenxin Li, Hengyu Liu, Yifan Liu, Brandon Y Feng, Wuyang Li, Xinyu Liu, Zhen Chen, Jing Shao, and Yixuan Yuan. Endora: Video generation models as endoscopy simulators. arXiv preprint arXiv:2403.11050, 2024.
- Xiang Lisa Li and Percy Liang. Prefix-tuning: Optimizing continuous prompts for generation. arXiv preprint arXiv:2101.00190, 2021.

- Xinmiao Lin, Yikang Li, Jenhao Hsiao, Chiuman Ho, and Yu Kong. Catch missing details: Image reconstruction with frequency augmented variational autoencoder. In Proceedings of the IEEE/CVF Conference on Computer Vision and Pattern Recognition, pp. 1736–1745, 2023.
- Jiaming Liu, Rushil Anirudh, Jayaraman J Thiagarajan, Stewart He, K Aditya Mohan, Ulugbek S Kamilov, and Hyojin Kim. Dolce: A model-based probabilistic diffusion framework for limited-angle ct reconstruction. In Proceedings of the IEEE/CVF International Conference on Computer Vision, pp. 10498–10508, 2023.
- Ze Liu, Jia Ning, Yue Cao, Yixuan Wei, Zheng Zhang, Stephen Lin, and Han Hu. Video swin transformer. In Proceedings of the IEEE/CVF conference on computer vision and pattern recognition, pp. 3202–3211, 2022.
- I Loshchilov. Decoupled weight decay regularization. arXiv preprint arXiv:1711.05101, 2017.
- Xin Ma, Yaohui Wang, Gengyun Jia, Xinyuan Chen, Ziwei Liu, Yuan-Fang Li, Cunjian Chen, and Yu Qiao. Latte: Latent diffusion transformer for video generation. arXiv preprint arXiv:2401.03048, 2024.
- Pablo Mesejo, Daniel Pizarro, Armand Abergel, Olivier Rouquette, Sylvain Beorchia, Laurent Poincloux, and Adrien Bartoli. Computer-aided classification of gastrointestinal lesions in regular colonoscopy. IEEE transactions on medical imaging, 35(9):2051–2063, 2016.
- Shentong Mo and Yapeng Tian. Scaling diffusion mamba with bidirectional ssms for efficient image and video generation. arXiv preprint arXiv:2405.15881, 2024.
- Chinedu Innocent Nwoye, Cristians Gonzalez, Tong Yu, Pietro Mascagni, Didier Mutter, Jacques Marescaux, and Nicolas Padoy. Recognition of instrument-tissue interactions in endoscopic videos via action triplets. In Medical Image Computing and Computer Assisted Intervention–MICCAI 2020: 23rd International Conference, Lima, Peru, October 4–8, 2020, Proceedings, Part III 23, pp. 364–374. Springer, 2020.
- Chinedu Innocent Nwoye, Tong Yu, Cristians Gonzalez, Barbara Seeliger, Pietro Mascagni, Didier Mutter, Jacques Marescaux, and Nicolas Padoy. Rendezvous: Attention mechanisms for the recognition of surgical action triplets in endoscopic videos. Medical Image Analysis, 78:102433, 2022.
- Muzaffer Özbey, Onat Dalmaz, Salman UH Dar, Hasan A Bedel, Şaban Öztürk, Alper Güngör, and Tolga Çukur. Unsupervised medical image translation with adversarial diffusion models. IEEE Transactions on Medical Imaging, 2023.
- Jinyoung Park, Hee-Seon Kim, Kangwook Ko, Minbeom Kim, and Changick Kim. Videomamba: Spatio-temporal selective state space model. arXiv preprint arXiv:2407.08476, 2024.
- Chenyang Qi, Xiaodong Cun, Yong Zhang, Chenyang Lei, Xintao Wang, Ying Shan, and Qifeng Chen. Fatezero: Fusing attentions for zero-shot text-based video editing. In Proceedings of the IEEE/CVF International Conference on Computer Vision, pp. 15932–15942, 2023.
- Alec Radford, Jong Wook Kim, Chris Hallacy, Aditya Ramesh, Gabriel Goh, Sandhini Agarwal, Girish Sastry, Amanda Askell, Pamela Mishkin, Jack Clark, et al. Learning transferable visual models from natural language supervision. In International conference on machine learning, pp. 8748–8763. PMLR, 2021.
- Aditya Ramesh, Mikhail Pavlov, Gabriel Goh, Scott Gray, Chelsea Voss, Alec Radford, Mark Chen, and Ilya Sutskever. Zero-shot text-to-image generation. In International conference on machine learning, pp. 8821–8831. Pmlr, 2021.
- Robin Rombach, Andreas Blattmann, Dominik Lorenz, Patrick Esser, and Björn Ommer. High-resolution image synthesis with latent diffusion models. In Proceedings of the IEEE/CVF conference on computer vision and pattern recognition, pp. 10684–10695, 2022.
- Masaki Saito, Eiichi Matsumoto, and Shunta Saito. Temporal generative adversarial nets with singular value clipping. In Proceedings of the IEEE international conference on computer vision, pp. 2830–2839, 2017.

- Xiaoqian Shen, Xiang Li, and Mohamed Elhoseiny. Mostgan-v: Video generation with temporal motion styles. In Proceedings of the IEEE/CVF Conference on Computer Vision and Pattern Recognition, pp. 5652–5661, 2023.
- Xiaoyu Shi, Zhaoyang Huang, Weikang Bian, Dasong Li, Manyuan Zhang, Ka Chun Cheung, Simon See, Hongwei Qin, Jifeng Dai, and Hongsheng Li. Videoflow: Exploiting temporal cues for multi-frame optical flow estimation. In Proceedings of the IEEE/CVF International Conference on Computer Vision, pp. 12469–12480, 2023.
- Uriel Singer, Adam Polyak, Thomas Hayes, Xi Yin, Jie An, Songyang Zhang, Qiyuan Hu, Harry Yang, Oron Ashual, Oran Gafni, et al. Make-a-video: Text-to-video generation without text-video data. arXiv preprint arXiv:2209.14792, 2022.
- Ivan Skorokhodov, Sergey Tulyakov, and Mohamed Elhoseiny. Stylegan-v: A continuous video generator with the price, image quality and perks of stylegan2. In Proceedings of the IEEE/CVF conference on computer vision and pattern recognition, pp. 3626–3636, 2022.
- Jimmy TH Smith, Andrew Warrington, and Scott W Linderman. Simplified state space layers for sequence modeling. arXiv preprint arXiv:2208.04933, 2022.
- Jascha Sohl-Dickstein, Eric Weiss, Niru Maheswaranathan, and Surya Ganguli. Deep unsupervised learning using nonequilibrium thermodynamics. In International conference on machine learning, pp. 2256–2265. PMLR, 2015.
- Jiaming Song, Chenlin Meng, and Stefano Ermon. Denoising diffusion implicit models. arXiv preprint arXiv:2010.02502, 2020.
- Liyao Tang, Zhe Chen, Shanshan Zhao, Chaoyue Wang, and Dacheng Tao. All points matter: entropy-regularized distribution alignment for weakly-supervised 3d segmentation. Advances in Neural Information Processing Systems, 36, 2024.
- Antti Tarvainen and Harri Valpola. Mean teachers are better role models: Weight-averaged consistency targets improve semi-supervised deep learning results. Advances in neural information processing systems, 30, 2017.
- Zachary Teed and Jia Deng. Raft: Recurrent all-pairs field transforms for optical flow. In Computer Vision–ECCV 2020: 16th European Conference, Glasgow, UK, August 23–28, 2020, Proceedings, Part II 16, pp. 402–419. Springer, 2020.
- Yu Tian, Guansong Pang, Fengbei Liu, Yuyuan Liu, Chong Wang, Yuanhong Chen, Johan Verjans, and Gustavo Carneiro. Contrastive transformer-based multiple instance learning for weakly supervised polyp frame detection. In International Conference on Medical Image Computing and Computer-Assisted Intervention, pp. 88–98. Springer, 2022.
- Andru P Twinanda, Sherif Shehata, Didier Mutter, Jacques Marescaux, Michel De Mathelin, and Nicolas Padoy. Endonet: a deep architecture for recognition tasks on laparoscopic videos. IEEE transactions on medical imaging, 36(1):86–97, 2016.
- Thomas Unterthiner, Sjoerd Van Steenkiste, Karol Kurach, Raphael Marinier, Marcin Michalski, and Sylvain Gelly. Towards accurate generative models of video: A new metric & challenges. arXiv preprint arXiv:1812.01717, 2018.
- Jiuniu Wang, Hangjie Yuan, Dayou Chen, Yingya Zhang, Xiang Wang, and Shiwei Zhang. Modelscope text-to-video technical report. arXiv preprint arXiv:2308.06571, 2023.
- Zhenbin Wang, Mao Ye, Xiatian Zhu, Liuhan Peng, Liang Tian, and Yingying Zhu. Metateacher: Coordinating multi-model domain adaptation for medical image classification. Advances in Neural Information Processing Systems, 35:20823–20837, 2022.
- Zhenbin Wang, Lei Zhang, Lituan Wang, and Zhenwei Zhang. Soft masked mamba diffusion model for ct to mri conversion. arXiv preprint arXiv:2406.15910, 2024.

- Jay Zhangjie Wu, Yixiao Ge, Xintao Wang, Stan Weixian Lei, Yuchao Gu, Yufei Shi, Wynne Hsu, Ying Shan, Xiaohu Qie, and Mike Zheng Shou. Tune-a-video: One-shot tuning of image diffusion models for text-to-video generation. In Proceedings of the IEEE/CVF International Conference on Computer Vision, pp. 7623–7633, 2023.
- Jinxi Xiang, Ricong Huang, Jun Zhang, Guanbin Li, Xiao Han, and Yang Wei. Versvideo: Leveraging enhanced temporal diffusion models for versatile video generation. In The Twelfth International Conference on Learning Representations, 2023a.
- Weilai Xiang, Hongyu Yang, Di Huang, and Yunhong Wang. Denoising diffusion autoencoders are unified self-supervised learners. In Proceedings of the IEEE/CVF International Conference on Computer Vision, pp. 15802–15812, 2023b.
- Jinbo Xing, Menghan Xia, Yuxin Liu, Yuechen Zhang, Yong Zhang, Yingqing He, Hanyuan Liu, Haoxin Chen, Xiaodong Cun, Xintao Wang, et al. Make-your-video: Customized video generation using textual and structural guidance. IEEE Transactions on Visualization and Computer Graphics, 2024a.
- Zhen Xing, Qi Dai, Han Hu, Zuxuan Wu, and Yu-Gang Jiang. Simda: Simple diffusion adapter for efficient video generation. In Proceedings of the IEEE/CVF Conference on Computer Vision and Pattern Recognition, pp. 7827–7839, 2024b.
- Zhuoyi Yang, Jiayan Teng, Wendi Zheng, Ming Ding, Shiyu Huang, Jiazheng Xu, Yuanming Yang, Wenyi Hong, Xiaohan Zhang, Guanyu Feng, et al. Cogvideox: Text-to-video diffusion models with an expert transformer. arXiv preprint arXiv:2408.06072, 2024.
- Sihyun Yu, Sangkyung Kwak, Huiwon Jang, Jongheon Jeong, Jonathan Huang, Jinwoo Shin, and Saining Xie. Representation alignment for generation: Training diffusion transformers is easier than you think. arXiv preprint arXiv:2410.06940, 2024.
- Mingliang Zhai, Xuezhi Xiang, Ning Lv, and Xiangdong Kong. Optical flow and scene flow estimation: A survey. Pattern Recognition, 114:107861, 2021.
- Richard Zhang, Phillip Isola, Alexei A Efros, Eli Shechtman, and Oliver Wang. The unreasonable effectiveness of deep features as a perceptual metric. In Proceedings of the IEEE conference on computer vision and pattern recognition, pp. 586–595, 2018.
- Daquan Zhou, Weimin Wang, Hanshu Yan, Weiwei Lv, Yizhe Zhu, and Jiashi Feng. Magicvideo: Efficient video generation with latent diffusion models. arXiv preprint arXiv:2211.11018, 2022.